PHYSICAL REVIEW FLUIDS **11**, 084505 (2026)

Arrested development of the Rayleigh-Taylor instability in the cabbeling regime

Marek Stastna *
Department of Applied Mathematics, University of Waterloo, Waterloo, Ontario N2L 3G1, Canada

Andrew P. Grace
Department of Applied Mathematics, University of Colorado Boulder, Boulder, Colorado 80309, USA

(Received 6 November 2025; accepted 15 July 2026; published 31 August 2026)

The fresh water equation of state exhibits a fundamentally important nonlinearity; the temperature at which it attains its maximum density occurs at roughly 4° C as opposed to at 0° C. The form of the equation of state in this regime is quadratic and has the well-known implication that two fluid parcels may mix and produce a child parcel with a higher density; a process known as cabbeling. In this work we report on direct numerical simulations of the Rayleigh-Taylor instability in the cabbeling regime. We demonstrate that the mature, three-dimensional state of the instability leads to cabbeling, which, in turn, serves to sustain an instability that would otherwise saturate outside of the cabbeling regime. We present a new quantitative measure of strong cabbeling potential and use it, along with the mechanical energy, to demonstrate that the Rayleigh-Taylor instability is arrested in two ways that are unique to the cabbeling regime. Our results have implications for radiatively driven, under-ice flows in late winter during which ice prevents mechanical driving by the wind. While our focus is on the freshwater setting, we extend the derivation of the strong cabbeling potential to heat-salt systems, thereby extending its usefulness to the broader community.

DOI: 10.1103/6m6k-tkjy

I. INTRODUCTION

Rayleigh-Taylor instability (henceforth RTI) is one of the canonical examples of transition to turbulence [1,2] in a stratified fluid. The instability is driven by an unstable buoyancy gradient, for example, rapidly overturning a glass of water (the dense fluid) in air (the light fluid), or when water below the temperature of maximum density is heated by radiation passing through overlying ice [3]. Rayleigh-Taylor instability has a broad research community spanning experimental [4,5], and numerical [6–8] approaches. In the field, RTI is often associated with convection due to radiative forcing, and the associated motions are often inferred from measurements of quantities relevant to the field campaign. An example are under-ice motions in Lake Simcoe, Canada, inferred based on dissolved oxygen measurements by the authors of [9]. While both layered (i.e., as distinct layers with discontinuous profiles of temperature and density across layer interfaces) and continuously stratified approaches have representation in the literature, we focus on the continuously stratified case.

The vigour of an RTI is largely set by the dimensionless density difference across the unstable interface. This is labeled the Atwood number and the literature contains examples of both large [10] and small Atwood number [4]. In ice-covered freshwater bodies of water toward the end of the winter, a regime of water colder than the temperature of maximum density (roughly 4°C) is

*Contact author: mmstastn@uwaterloo.ca

often observed [9,11]. For this temperature range the representative Atwood number is roughly two orders of magnitude smaller than laboratory examples [4]. As solar radiation penetrates the overlying ice, the fluid column is destabilized in the near-surface layer. With continued heating, the water column reaches a point in which fluid parcels of identical densities on either side of the approximately parabolic equation of state are present. This implies that two fluid parcels of identical density can mix to produce a child parcel that is denser than both parents a process known as cabbeling. Cabbeling may be further subdivided into two types, one in which the nonlinear equation of state implies that $\rho_{\text{child}} \neq 0.5(\rho_{\text{parent1}} + \rho_{\text{parent2}})$ and a smaller subset in which $\rho_{\text{child}} > \max(\rho_{\text{parent1}}, \rho_{\text{parent2}})$. Historically, the distinction was not always clear in the literature. In [12], the authors interpreted cabbeling by the more restrictive definition. The above subdivision was recognized in [13], though no consistent terminology was adopted in the literature. Based on discussions in the large-scale oceanographic literature [14], Grace *et al.* [15] suggested that the case in which $\rho_{\text{child}} > \max(\rho_{\text{parent1}}, \rho_{\text{parent2}})$ should be referred to as *strong cabbeling* due to the possibility of mixing leading to new local maxima of density, and hence a stronger influence on local dynamics. The same authors argued that the case for which $\rho_{\text{parent1}} < \rho_{\text{child}} < \rho_{\text{parent2}}$ should be referred to as *weak cabbeling* because no new local density maximum are introduced via mixing. Weak cabbeling has been shown to affect the detailed dynamics of both gravity currents [15,16] and shear instabilities [17] on the laboratory scale. At the field scale, cabbeling is believed to play an important role in controlling mixing processes between river inflow and lakes below the temperature of maximum density [18].

Experimentally realized RTI typically begins with a pre-existing reservoir of potential energy that is subsequently converted to kinetic energy. Strong cabbeling can create new, local regions of instability when two fluid parcels on opposite sides of the temperature of maximum density mix. This implies that mixing induced by the instability can serve as a "bootstrap" for further instability and further mixing. Therefore, strong cabbeling serves as a distinct mechanism that drives the continual development of RTI. An alternative interpretation would identify strong cabbeling as a wholly new instability. We choose to keep the term RTI as a description of all instances of locally unstable density gradients, whether due to initial conditions or strong cabbeling. Due to the extremely small density differences (on the order of $0.1\,\text{kg}\,\text{m}^{-3}$) that typify the cold water regime, mechanical energy is expected to be dominant, but buoyancy cannot be neglected since it is the *sine qua non* of the instability. The nonmonotonicity of the equation of state provides novel exchange pathways between kinetic and potential energy. These need to be incorporated into the sorting method for separating available and background potential energy [3,19–22]). Of these, the authors of [21] provided a concrete accounting for the nonlinear equation of state and the radiative forcing (e.g., their Fig. 3), though the topic of strong cabbeling is not explicitly mentioned. Indeed, mixing in the context of the nonlinear equation of state, such as in descriptions of the deep ocean (for which all of the salinity, temperature, and pressure impact density) is a rich subject. Tailleux has considered the problem in a number of works [22–24]. In an independent study, Nycander [25] considered the problem of energy conversion under a nonlinear equation of state using the concept of neutral surfaces. Given that it is the strong cabbeling that works to enhance the vigor of the RTI, the central questions we aim to answer are somewhat more localized.

(1) Can the local occurrence of strong cabbeling be tracked using a computationally simple measure/algorithm?

(2) Can this algorithm be applied to discriminate between conditions under which cabbeling drives a mature (i.e., late time), three-dimensional RTI, and those in which the RTI is arrested?

(3) Can this algorithm be generalized to the oceanic setting in which density depends on temperature and salinity.

The first and third questions are answered by constructing what we call the strong cabbeling potential and providing an algorithm for its calculation. To answer the second question, we employ pseudospectral numerical simulations [26] to demonstrate that strong cabbeling can drive RTI that would saturate at the same Atwood number outside the cabbeling regime. The new strong cabbeling potential measure and standard energetics are subsequently used to demonstrate a unique type of

TABLE I. The list of constant parameters used in this study, their values, dimensions, and a description.

Parameter symbol	Value	Dimensions	Description
g	9.81	$\mathrm{m/s^2}$	Acceleration due to gravity
$\tilde{T}_{md}$	3.98	$^\circ\mathrm{C}$	Temperature of maximum density
ρ_0	999.974	$\mathrm{kg/m^3}$	Constant reference density
γ	7.6×10^{-6}	$^\circ\mathrm{C}^{-2}$	NLEOS constant
L	0.256	m	Side length of cubical domain
Pr	7		Prandtl Number
ν	1.0×10^{-6}	$\mathrm{m^2/s}$	Kinematic viscosity
κ	0.1429×10^{-6}	$\mathrm{m^2/s}$	Tracer diffusivity

arrested development of the RTI in the strong cabbeling regime. Our results have implications for mixing in natural waters over the late winter/early spring, while the new measure of strong cabbeling potential can be applied for any flow in the strong cabbeling regime.

II. METHODS

We employ the pesudospectral solver spins [26] to solve the incompressible Navier-Stokes equations under the Boussinesq approximation (i.e., p is the perturbation pressure)

$$\begin{aligned} \rho_0 \frac{D\vec{u}}{Dt} &= -\nabla p - \rho(\tilde{T})g + \mu \nabla^2 \vec{u}, \\ \nabla \cdot \vec{u} &= 0, \\ \frac{D\tilde{T}}{Dt} &= \kappa \nabla^2 \tilde{T}, \end{aligned} \tag{1}$$

in a rectangular prism of size L^3, where L is the vertical extent. After a set of preliminary simulations we settled on $L = 0.256$ m and a grid resolution of 5×10^{-4} m, which implies that the simulations can be considered to be DNS. It is worth noting that the Reynolds number of our situation is too low for isotropic homogeneous turbulence to be realized. As we are focused primarily on the dynamics away from boundaries, we have chosen to employ free-slip boundary conditions for velocity along all walls, and no-flux boundary conditions for temperature. In this work, the departure of density from its reference state ρ_0 (Table I) is approximated by a quadratic fit [7,27]

$$\rho = -\gamma(\tilde{T} - \tilde{T}_{md})^2 \tag{2}$$

to the freshwater, surface-pressure limit of the equation of state of McDougall *et al.* [28]. As such, this expression is suitable for cold, fresh water less than approximately 10° C [27]. Here $\tilde{T}$ is the dimensional temperature, and $\tilde{T}_{md}$ is the temperature of maximum density. We define $\Delta\tilde{T}$ as the absolute maximum temperature change from $\tilde{T}_{md}$ in the initial conditions, and γ is a fitting constant (value shown in Table I) proportional to the temperature derivative of the thermal expansion coefficient. The temperature field is scaled as

$$T = \frac{\tilde{T} - \tilde{T}_{md}}{\Delta\tilde{T}} \tag{3}$$

so that the dimensionless temperature range for initial conditions symmetric about the temperature of maximum density is ± 1. The vertical extent of the tank L is a reasonable choice of a characteristic length scale, and a characteristic time can be defined using the phenomenological, quadratic scaling of Clark [6] as the time for the interface to grow to one tenth of the vertical extent of the domain. This choice is motivated by the desire to choose a timescale relevant to the mature stage of the instability and not its initial growth, though we note that it is not unique. It should, however,

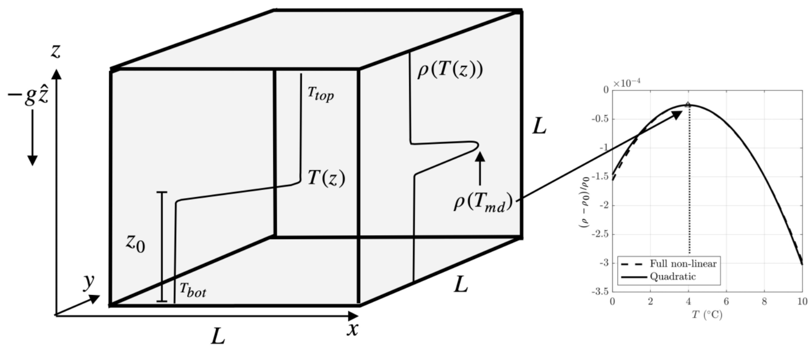

FIG. 1. A schematic representation of the initial temperature and density profiles, as well as the geometric of the numerical domain. The temperature profile crosses T_{md}, which is highlighted in the plot of the nonlinear equation of state on the right.

be readily realizable in the laboratory; a major factor in our choice of configuration since strong cabbeling is understudied from an experimental point of view. The Reynolds number based on the above choices of scales is $O(10^3)$, which is confirmed *a posteriori* using the root mean square speed of a mature state in the simulations. The Atwood number is defined as

$$At = \frac{\rho_{\max} - \rho_{\min}}{\rho_0} \tag{4}$$

and for the simulations presented below can be estimated as $At \approx 6.6 \times 10^{-5}$. As noted in the Sec. I, this is several orders of magnitude smaller than experimental realizations in the literature [4]. In this work, we consider an initially quiescent flow for which the temperature distribution takes the form

$$\tilde{T}(x, y, z, t = 0) = T_{\text{bot}} + (T_{\text{top}} - T_{\text{bot}})\tfrac{1}{2}\{1 + \tanh[(z - z_0)/d]\}, \tag{5}$$

with T_{bot} and T_{top} chosen so that $\rho(T_{\text{bot}}) = \rho(T_{\text{top}})$. The temperature at the center of the interface is the temperature of maximum density. Three different interface heights, $z_0 = (0.125, 0.5, 0.875)$ (dimensionless) are considered, to investigate the efficacy of cabbeling as a mechanism for mixing. All cases are statically unstable. Since it is known from previous work, i.e., Grace *et al.* [27,29], that cabbeling is a highly nonlinear and spatially nonlocal mixing mechanism, we expect the proximity of the unstable layer to the boundaries to play a nontrivial role in the dynamics *a priori* as the boundaries can limit the growth of the instabilities and modify the overall state of mixing. The setup is schematized in Fig. 1.

An equation for the density can be constructed from the temperature equation and the equation of state

$$\frac{D\rho}{Dt} = \kappa\nabla^2\rho + 2\gamma\kappa|\nabla T|^2. \tag{6}$$

The second term on the right-hand side corresponds to the effect of cabbeling. However, it is agnostic as to the actual temperature value (i.e., one can add an arbitrary constant value to T while leaving $|\nabla T|^2$ unchanged). It thus does not discriminate between strong and weak cabbeling.

To quantify the role of strong cabbeling, we define a measure of strong cabbeling potential, labeled Φ, defined in the following manner. If we let $T(\vec{x})$ represent the temperature at a specified location in a three-dimensional space, and $T(\vec{x} + \vec{r})$ represent the temperature at a location $\vec{x} + \vec{r}$, we can define a quantity S, such that

$$S = \frac{1}{2} - \frac{1}{2}\text{sign}\left(\frac{T(\vec{x} + \vec{r})}{T(\vec{x})}\right), \tag{7}$$

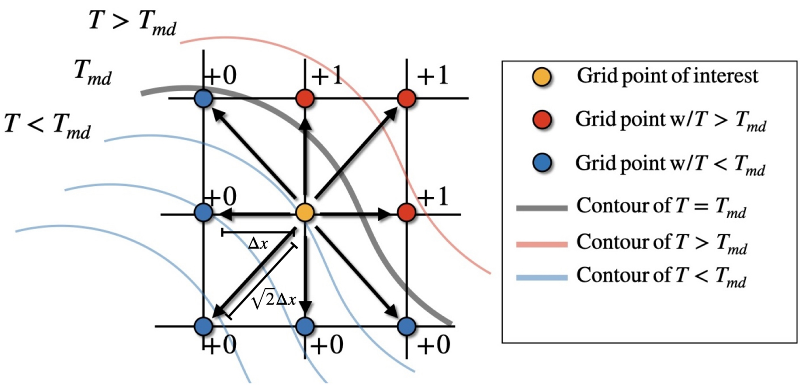

FIG. 2. Diagram demonstrating the calculation of the strong cabbeling potential Φ in two dimensions for simplicity.

where sign$(\cdot)$ returns 1 if the sign of the argument is positive, identically zero, or undefined [i.e., $T(\vec{x}+\vec{r})$ or $T(\vec{x})$ are zero], and -1 if the sign of the argument is negative. Therefore, if the (nondimensional) temperatures measured at a separation $\vec{r}$ are of opposite signs (meaning cabbeling will occur), then S takes on a value of 1, and takes on a value of zero in all other cases. Therefore, we define the strong cabbeling potential on a scale $\vec{r}$, as

$$\Phi(r) = \langle S \rangle_r, \tag{8}$$

where the notation $\langle \cdot \rangle_{\vec{r}}$ represents an average conditioned on the separation vector $\vec{r}$. Φ is ultimately an average of a binary measure, and its magnitude represents a measure of how active cabbeling is on a scale $\|r\|$. In principle, the strong cabbeling potential could be applied to any separation distance (and could therefore be related to the spatial correlations of the temperature field and the spectra of the temperature fluctuations), but since we are only concerned with $\|r\| = \mathcal{O}(\Delta x)$ (i.e., on the order of the numerical grid spacing), then $\Phi = \langle S \rangle_{\Delta x}$ where Δx is fixed. In practice, we compute Φ according to the following algorithm.

The algorithm is schematized in Fig. 2.

Relative to the primary point of interest, grid points are either located at a distance $\sqrt{3}\Delta x$, $\sqrt{2}\Delta x$, or Δx, due to the uniform rectilinear grid. However, as the flow is well resolved (discussed earlier), the errors associated in this difference in the evaluation do not change the conclusions of this work.

Figure 3 demonstrates how the strong cabbeling potential is novel. Figure 3(a) shows the temperature field for a shear instability in sub-four degree water for which only weak cabbeling is possible. This configuration was studied in [17], and the reader is directed to this article for detailed consideration of the dynamics. For the present purposes, the essential point to note is that by construction Φ, the strong cabbeling potential, is identically zero. In Fig. 3(b), we show the cabbeling diagnostic from the density equation (6). The values are clearly nonzero, and hence if one is interested in identifying regions of strong cabbeling, this diagnostic may not prove helpful (though it does have the advantage of a direct link to the sorting algorithm characetrization of bulk mixing [21]). We will return to this discussion in the Sec. III.

The focus for the present work is on the freshwater situation for which $\rho(T)$, it is worth noting that the strong cabbeling potential may be generalized to the situation for which $\rho(s, T)$, where s is the salinity. For the majority of oceanic situations the range of observed salinity is high enough to preclude nonmonotonocity in the equation of state. However, for brackish waters nonmonotonocity is still possible. Indeed measurements in small Arctic lakes suggest salinity plays a dynamical role in springtime mixing [30], and [31] have shown experimentally that salt-fingering is possible in a slowly chilled tank of water representative of a subset of lake conditions. The key observation is that in the subdomain of $s - T$ space for which cabbeling is possible s acts to shift the parabola

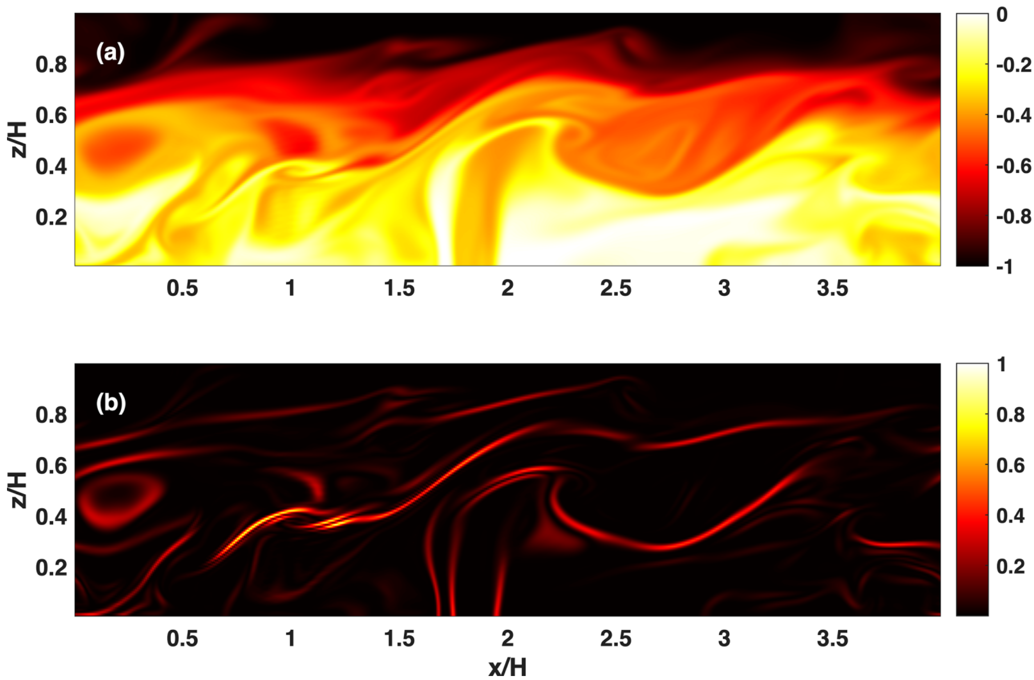

FIG. 3. (a) The scaled temeprature of the mature stage of the KH instability in the cold water (sub-four degree) regime for which ONLY weak cabbeling is possible. See [17] for more details of the simulations. (b) The cabbeling diagnostic from Eq. (6). Φ is identically zero for this simulation.

observed in the pure $\rho(T)$ case. This means that a curve C can be defined, for which the maximum density for a given salinity value is achieved (see Fig. 4). The algorithm above is then generalized as follows.

Regardless of whether one is working in the freshwater (T only), or oceanic ($s - T$) setting, the point of the above derivation is that the potential for cabbeling to take place can be defined

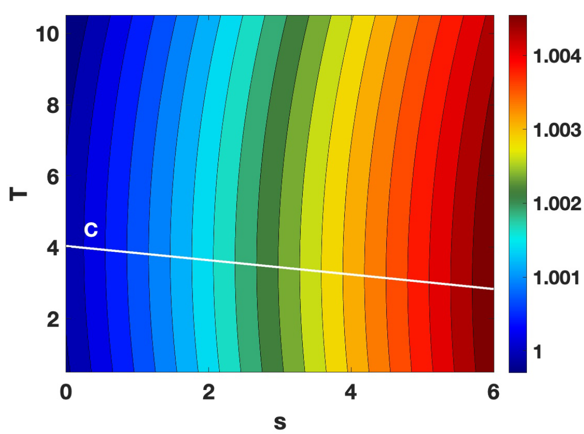

FIG. 4. Shaded contours of density in $s - T$ space with the curve C at which the maximum density occurs in white. This curve is needed to calculate the strong cabbeling potential in situations in which both salinity and temperature are important

ALGORITHM 1. The strong cabbeling potential algorithm for an equation state that is a function of temperature only.

(1) Choose a point and loop over its 26 neighbors (8 for a two dimensional simulation) on the computational grid.
(2) For each neighbor determine if the original point and the neighbor lie on opposite sides of the temperature of maximum density. If so add one to Φ.
(3) Divide Φ by 26 (or 8 for a two dimensional simulation) to get a fraction of strong cabbeling potential.

locally (i.e., pointwise) or in various integrated forms (e.g., as a horizontal total at a fixed z value). As constructed, the strong cabbeling potential does not account for the strength of cabbeling. In previous work [32] we reported on the fraction of the computational domain that is within a fixed percentage of the maximum density. This gives some indication of cabbeling, though the present computational algorithm (Algorithm 1 in practice) has the advantage that it ensures cabbeling will actually take place. Moreover, it works for all data pairs, with no restriction of points near the temperature of maximum density. We believe this diagnostic, and its extension to thermohaline systems which we also give above, could be useful for a far broader set of applications than the RTI studied herein, such as the study of CO_2 mixing in multiphase systems [33,34].

III. RESULTS

We begin by contrasting the mature state of the RTI for cases with cabbeling and outside of the cabbeling regime. For the noncabbeling case the temperature range was adjusted so as to match the initial state for density in the cabbeling case (similarly to the shear instability case studied in [32]). Figure 5 shows both quantitative and qualitative comparisons. Figure 5(a) shows the horizontally

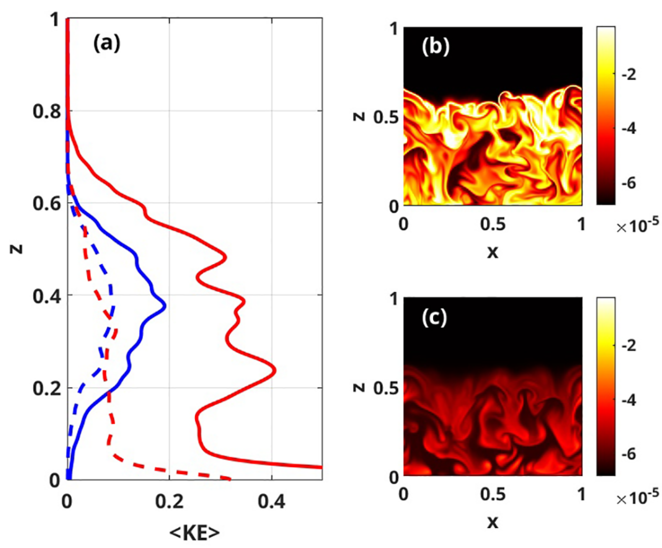

FIG. 5. Summary comparison of cabbeling RT and RT outside cabbeling regime. (a) Horizontally averaged KE at $t = 3.36$ (blue) and $t = 5.04$ (red); signals from the cabbeling case are indicated by solid lines. Note that all signals are scaled by the maximum of the solid red curve, (b) Nondimensional density difference from the reference density at $t = 5.04$ for the cabbeling RT case, and (c) Nondimensional density difference from the reference density at $t = 5.04$ for the noncabbeling RT case.

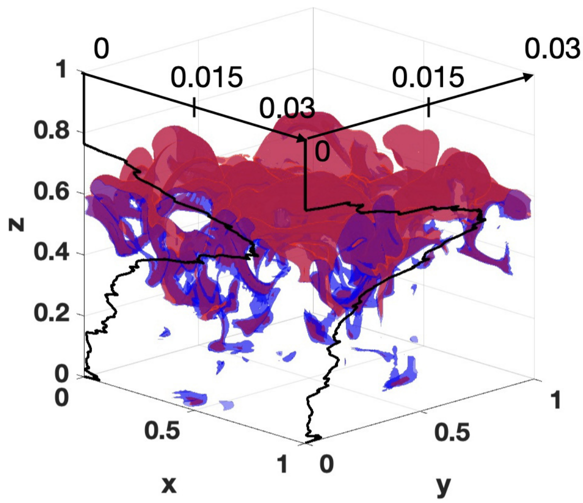

FIG. 6. Two isosurfaces of temperature on either side of the temperature of maximum density ($T = \pm 0.1$) at time $t = 5.04$. Overlaid along the $y = 0$ and $x = 1$ planes are plots of the total strong cabbeling potential fraction Φ at each height z (the upper axes show the extent of Φ).

averaged kinetic energy at two different times for the cabbeling (solid) and noncabbeling (dashed) cases. All curves have been scaled by the maximum value of the red solid curve (i.e., the cabbeling case at late time). It can be seen that for the earlier time shown, the two cases are comparable. However, the noncabbeling case quickly runs out of buoyancy to drive instability as the three-dimensional motions lead to rapid temperature mixing (and hence density homogenization). This is confirmed by contrasting Figs. 5(b) and 5(c) which show a slice of scaled density difference from the reference density in the center of the domain at $t = 5.04$. It is clear that there is a strong coupling between the RTI dynamics and the formation of dense water. Cabbeling drives the creation of dense water and this in turn energizes the instability over the bottom 60% of the domain, implying entrainment of fluid initially in the upper half of the domain has taken place.To get some intuition for the three-dimensionalized state and the role of cabbeling in it, Fig. 6 shows two isosurfaces of temperature near the temperature of maximum density at $t = 5.04$ for the case with the interface initially at the middepth. At this time, the RTI is fully three-dimensional and extends both upward via entrainment and downward due to sinking plumes of dense fluid. Overlaid on the isosurfaces (on the planes $y = 0$ and $x = 1$) are two plots of the total strong cabbeling potential Φ at each height z. The maximum value attained is roughly 0.02 and the profiles have been scaled so as to be visible on the scale of the isosurface (the axis for Φ is shown at the top of the plot).

Figure 7 provides an alternative view point by plotting the $x - z$ slices of excess density ($\sigma = \rho - 1000\,\mathrm{kg\,m^{-3}}$), strong cabbeling potential and the kintic energy. It is particularly poignant in demonstrating that while density and kinetic energy variations occupy large portions of the domain, the potential for cabbeling is much more localized.

Taken together, the two figures show unambiguously that while the downward spreading plumes lead to some enhanced cabbeling below the initial level of the density interface, it is the region where fluid from above the interface is entrained into the active RTI region that leads to the largest increase in strong cabbeling potential. It is this region in which the RTI is subsequently "boot-strapped" by cabbeling. It is worth noting that Φ identifies the beginning of the "boot-strapping," with the actual increase in kinetic energy occurring some time later. Moreover, Fig. 7 clearly indicates that Φ provides novel local information from both the density and KE fields.

The evolution of the horizontally integrated strong cabbeling potential as a function of z for three interface height cases is shown in Fig. 8 (40% of the domain in the vertical is shown). It can be seen

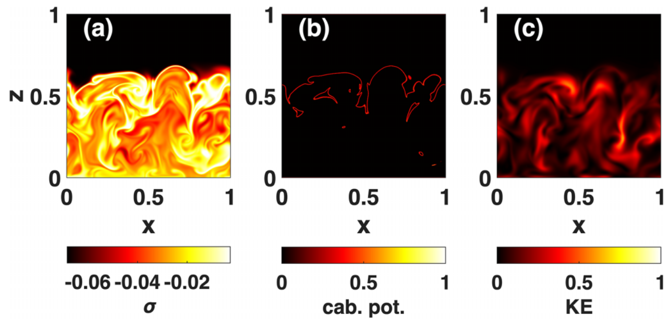

FIG. 7. $x - z$ slices at the same time as Fig. 6. (a) $\sigma = \rho - 1000\,\mathrm{kg\,m^{-3}}$, (b) strong cabbeling potential, Φ, scaled by its maximum possible value, and (c) kinetic energy scaled by its maximum

that the interface initially found at $z = 0.875$, Fig. 8(a), leads to a period of enhanced instability due to cabbeling, but as the upper layer is mixed out, cabbeling ceases entirely. In contrast the interface found initially at $z = 0.5$, Fig. 8(b), yields cabbeling for all times shown. Interestingly, the locus of cabbeling shifts upwards into the entrainment region, reaching above $z = 0.7$ by the end of the simulation. The case with the interface initially at $z = 0.125$, Fig. 8(c) yields the largest strong cabbeling potential values, but little to no entrainment from above. These results are intriguing, as they suggest a coupling between the upper and lower layers of the flow; the entrainment from above is influenced by the maturity of the instabilities which develop primarily downward. To relate the strong cabbeling potential to the sorted density profile used to define the background potential energy in energetics characterizations of mixing, Figs. 8(d)–8(f) show the horizontally averaged and adiabatically sorted density profiles for the three cases at $t = 8.4$. Following [19] z_* is the vertical coordinate for the sorted density profile. At this time, the near upper boundary interface case has evolved to a state with a weak, stable stratification (i.e., the RTI has been arrested), the middle interface case continues to exhibit an unstable overhang at the top of the entrainment layer (the RTI continues to be "boot-strapped" by cabbeling), while the near bottom interface case has a much smaller overhang at the top of what will be shown to be a far weaker entrainment layer.

Figure 9 shows histograms of the base 10 logarithm of the kinetic energy distribution at each z value for the three initial interface height cases. The time $t = 5.04$ has been chosen, though the results are representative of the mature state of the instability. The high interface case, Fig. 9(a),

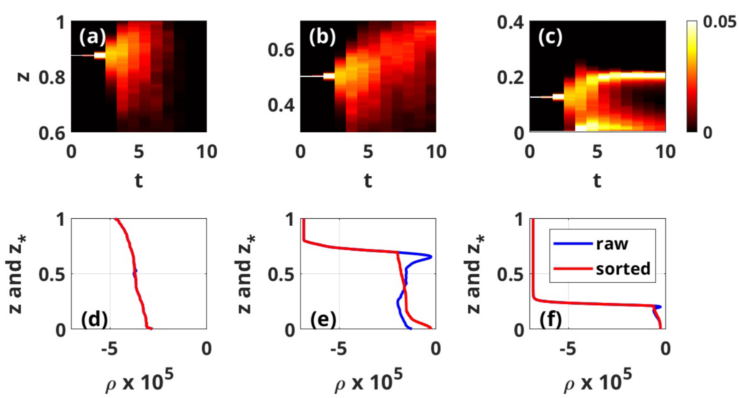

FIG. 8. Hovmöller plots (t versus z) of the strong cabbeling potential; Φ saturated on [0,1] (a)–(c), and plots of the horizontally averaged and sorted density profiles at $t = 8.4$ (d)–(f). (a) and (d) initial interface at 0.875, (b) and (e) initial interface at 0.5, (c) and (f) initial interface at 0.0125.

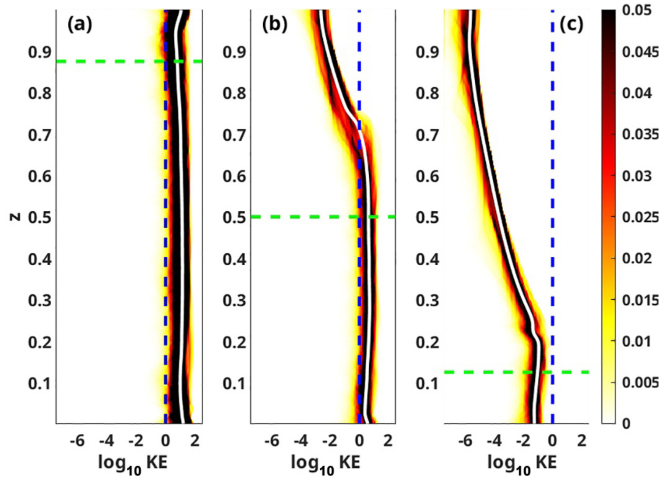

FIG. 9. Histogram of the base ten logarithm of the KE distribution at each z. $t = 5.04$. Initial interface indicated by green dashed line, the mean value by a white curve. (a) Initial interface at 0.875, (b) initial interface at 0.5, (c) initial interface at 0.0125. The value of $\log_{10} KE = 0$ is indicated by a blue dashed line.

leads to the systematically largest values of the kinetic energy. Moreover, the distribution is quite tight around the mean value which is indicated by a white curve (and such a tight distribution is observed for all cases). The RTI in its mature state has been energized by cabbeling and by the fact that individual plumes have room to sink and interact in a fully three-dimensionalized flow. Figure 9(b) shows the case with the initial interface at $z = 0.5$. This case yields a kinetic energy distribution that is similar to the $z = 0.875$ case in the region of active instability. This includes the bottom half of the domain as well as the region of entrained fluid above the middepth (below about $z = 0.75$). Above the entrainment region the kinetic energy rapidly decays, as entrainment by large scale instabilities becomes too weak to overcome the stable stratification appearing at the interface, which was studied in detail in [29]. Figure 9(c) shows the rather contrasting picture for the $z = 0.125$ case. Here the kinetic energy values are at least two orders of magnitude lower than both other cases and while some entrainment is evident, above $z = 0.25$ the kinetic energy decays rapidly. Thus a complete picture of the RTI in the cabbeling regime can only be established by considering both the kinetic energy and the potential for cabbeling. For example, in the $z = 0.875$ case, when the instability runs out of fuel to drive cabbeling, it has already reached a state over 100 times more energetic than that of the $z = 0.125$ interface. If there is either insufficient fuel for cabbeling, or room for plumes to reach a mature state, the RTI is arrested.

Finally, we return to the question of how different the characterizations of cabbeling due to the strong cabbeling potential and the density equation based method (the term proportional to $|\nabla T|^2$ often labeled χ in the literature) are in practice. Figure 10 shows the spanwise average of $|\nabla T|^2$ [Fig. 10(a)] and the strong cabbeling potential [Fig. 10(b)]. It can be seen that the spatial distribution is similar, though there are two clear differences, the most obvious is the vertical shift between the two, with details of the geometric structure (the strong cabbeling potential is more wispy in character). Figure 10(c) shows the horizontal average of the two scaled so as to lie on a common horiozn tal axis. It is clear that χ peaks systematically above the strong cabbeling potential. This is physically sensible since $|\boldsymbol{\nabla} T|$ will be nonzero before the temperature of maximum density is reached. The discrepancy is better quantified in Fig. 10(d) which shows the proportion of the areal domain at each z that has SCP above 0.1 but $\chi < 0.1$ (cyan) and that has χ above 0.1 but the strong cabbeling potential below 0.1 (magenta). It is clear that the two quantities give similar distributions, but with a clear and systematic difference. All panels are shown at $t = 5.04$, though the results were found to be consistent with other output times (not shown).

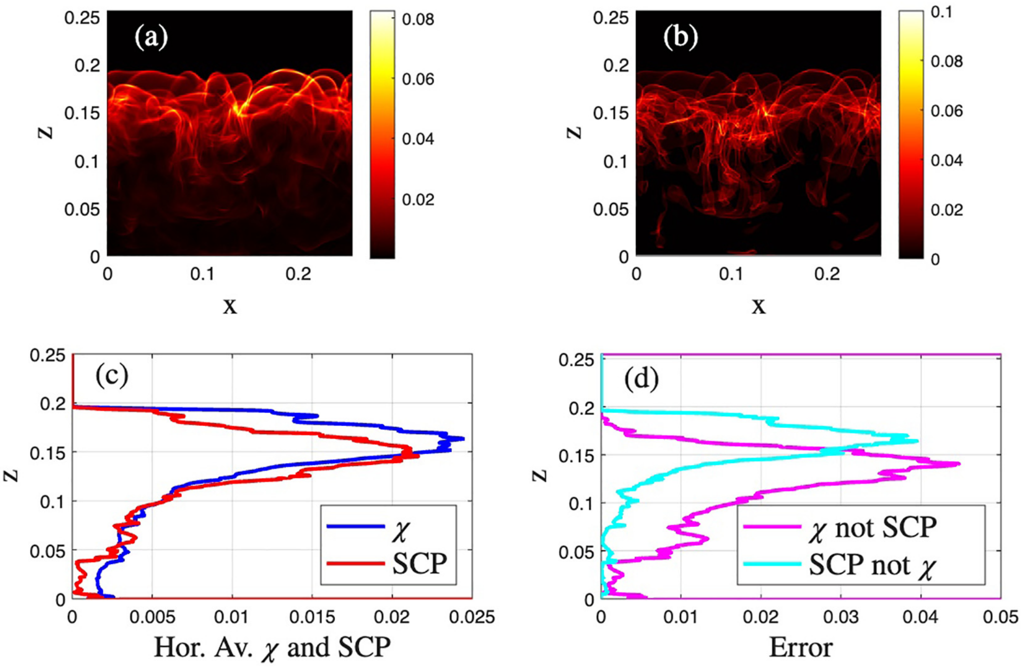

FIG. 10. (a) Spanwise average of $|\nabla T|^2$ scaled by its maximum value saturated on [0,0.08], (b) spanwise average of the strong cabbeling potential scaled by the highest possible value and saturated on [0,0.1]. (c) Horizontal mean of $|\nabla T|^2$ (blue) and the strong cabbeling potential (red) labeled as SCP in the legends, (d) error in the distribution of $|\nabla T|^2$ and the strong cabbeling potential, type 1 (magenta) type 2 (cyan). All panels at $t = 5.04$.

A user thus has the choice of using χ if they wish to make contact with sorting algorithm-based characterizations of bulk mixing (at the cost of not being able to differentiate between strong and weak cabbeling), or using the strong cabbeling potential if they want to identify regions of strong cabbeling (at the cost of losing the direct connection to bulk mixing).

IV. DISCUSSION

The cold water of regime of mid to high latitude lakes under late winter/early spring ice provides the setting for a unique type of stratified flow dynamics (e.g., [18,35]). On the one hand, the density differences (i.e., Atwood numbers) are very small, implying that while motions are three-dimensional they are not typified by the high Reynolds numbers common to virtually all other natural flows. On the other hand, the nonlinearity of the equation of state, and the resultant phenomenon of strong cabbeling, implies that motions have the potential to sustain themselves by mixing fluid parcels on opposite sides of the density versus temperature parabola, an effect absent outside of the strong cabbeling regime.

In the context of the RTI this implies that the vigor of the instability may be increased by strong cabbeling, while at the same time implying that the longevity of the instability depends on a reservoir of fluid that facilitates strong cabbeling. In practice, this implies that the strong cabbeling regime has two additional means by which the development of the RTI is arrested, in addition to the general scenario of "instability is quenched by diffusion." The three scenarios are summarized in diagram form in Fig. 11.

The diagrams have been augmented with profiles of the scaled temperature field at $t = 8.4$ in the (i) $x - z$, and (ii) $x - y$ planes. Since the color bar is chosen to be consistent between cases,

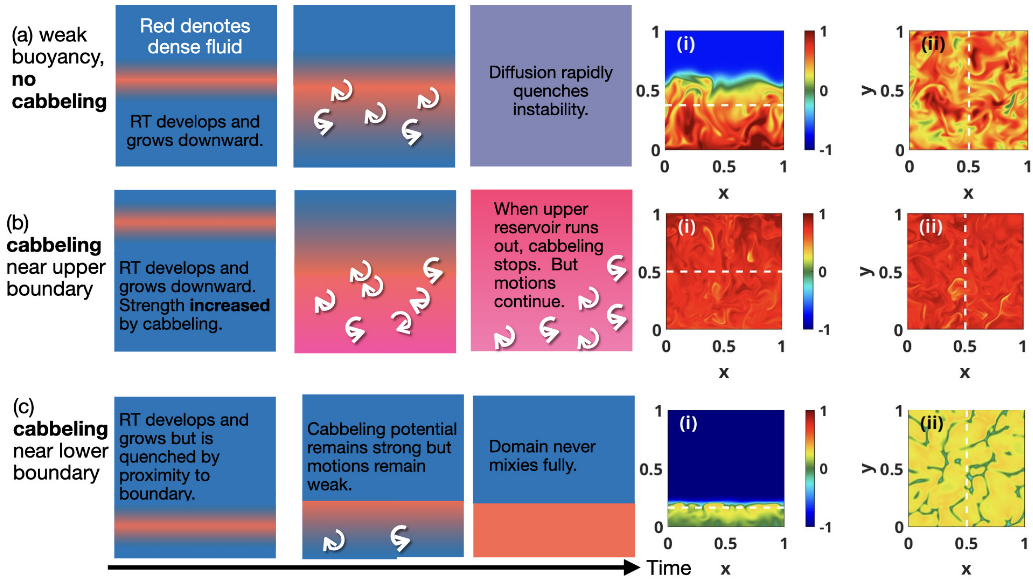

FIG. 11. Diagram of the three possible ways the development of the RTI is arrested. For each scenario representative $x-z$ and $x-y$ slices of the scaled temperature field are shown in subpanels (i) and (ii), respectively.

the range of colors demonstrates how efficiently the temperature field has been mixed. The outside-the-strong-cabbeling-regime case exhibits temperatures that span the whole range of dimensionless temperatures. However, since the density change is chosen to match that in the cold-water regime, the dimensional temperature changes are very small. This weaker response was also clear in the horizontally averaged kinetic energy profiles in Fig. 5. The near-upper-boundary-case shows a thoroughly mixed, warm fluid with some thin filaments, while the near-lower-boundary case exhibits a large, quiescent pool of cold fluid, and weak R-T instabilities with larger scales than the other two cases in the x-y plane. To discriminate between the scenarios in Figs. 11(b) and 11(c) we developed a novel measure of strong cabbeling potential Φ with the calculation method for this quantity summarized in Algorithm 1. This quantity, by design, uses the scalar actually advected by the numerical model, as opposed to a derived quantity such as density or buoyancy. The algorithm can be used locally, or in integrated form (e.g., over horizontal slices). Moreover, it is readily extensible to the oceanic $\rho(T, s)$ setting and hence we believe this quantity has utility well beyond the study of the RTI.

Future work should build on recent work on cabbeling in the context of heat-salt systems [36] and apply the extension of the strong cabbeling potential described in Algorithm 2 to this system. The

ALGORITHM 2. The strong cabbeling potential algorithm for an equation state that is a function of temperature and salinity.

(1) Define the curve C described above (i.e., using a fine grid in $s - T$ space).
(2) Choose a point in the computational domain and define the density ρ_{now} at this point.
(3) For each neighbor determine if the density at the neighbor point and ρ_{now} lie on opposite sides of the curve C. If so add one to Φ.
(4) Divide Φ by 26 (or 8 for a two dimensional simulation) to get a fraction of strong cabbeling potential.

spatially varying solar forcing of freshwater lakes [37] with overlying lake ice provides a different, applied research direction and would involve either Algorithm 1 or 2, depending on whether salinity is relevant in the particular lake context (see the discussion in [31]).

ACKNOWLEDGMENTS

M.S. gratefully acknowledges discussions with Nico Castro-Folker and Khush Bhavsar. M.S. acknowledges support from the Natural Sciences and Engineering Research Council of Canada (NSERC) via Discovery Grant No. RGPIN-311844-37157. A.P.G. acknowledges support from the NSERC Postdoctoral Fellowship Program.

DATA AVAILABILITY

Data that support the findings of this article are available by request from the corresponding authors, as well as case files for the SPINS software used to run all simulations.

[1] H.-J. Kull, Theory of the Rayleigh–Taylor instability, Phys. Rep. **206**, 197 (1991).

[2] P. Kundu, *Fluid Mechanics* (Elsevier, Amsterdam, 2016).

[3] H. N. Ulloa, A. Wüest, and D. Bouffard, Mechanical energy budget and mixing efficiency for a radiatively heated ice-covered waterbody, J. Fluid Mech. **852**, R1 (2018).

[4] M. J. Andrews and S. B. Dalziel, Small Atwood number Rayleigh–Taylor experiments, Philos. Trans. R. Soc. A **368**, 1663 (2010).

[5] T. J. McDougall, Double-diffusive convection with a nonlinear equation of state: Part II. Laboratory experiments and their interpretation, Prog. Oceanogr. **10**, 91 (1981).

[6] T. T. Clark, A numerical study of the statistics of a two-dimensional Rayleigh–Taylor mixing layer, Phys. Fluids **15**, 2413 (2003).

[7] J. Olsthoorn, E. W. Tedford, and G. A. Lawrence, Diffused-interface Rayleigh-Taylor instability with a nonlinear equation of state, Phys. Rev. Fluids **4**, 094501 (2019).

[8] A. Sengupta, H. N. Ulloa, and B. Joshi, Multi-layer Rayleigh-Taylor instability: Consequences for naturally occurring stratified mixing layers, Phys. Fluids **35**, 102110 (2023).

[9] B. Yang, J. Young, L. Brown, and M. Wells, High-frequency observations of temperature and dissolved oxygen reveal under-ice convection in a large lake, Geophys. Res. Lett. **44**, 12 (2017).

[10] I. Yilmaz, Analysis of Rayleigh-Taylor instability at high atwood numbers using fully implicit, non-dissipative, energy-conserving large eddy simulation algorithm, Phys. Fluids **32**, 054101 (2020).

[11] G. Kirillin, M. Leppäranta, A. Terzhevik, N. Granin, J. Bernhardt, C. Engelhardt, T. Efremova, S. Golosov, N. Palshin, P. Sherstyankin, G. Zdorovennova, and R. Zdorovennov, Physics of seasonally ice-covered lakes: A review, Aquat. Sci. **74**, 659 (2012).

[12] T. D. Foster and E. C. Carmack, Temperature and salinity structure in the Weddell Sea, J. Phys. Oceanogr. **6**, 36 (1976).

[13] T. J. McDougall, Thermobaricity, cabbeling, and water-mass conversion, J. Geophys. Res.: Oceans **92**, 5448 (1987).

[14] C. J. Shakespeare and L. N. Thomas, A new mechanism for mode water formation involving cabbeling and frontogenetic strain at thermohaline fronts. Part II: Numerical simulations, J. Phys. Oceanogr. **47**, 1755 (2017).

[15] A. P. Grace, M. Stastna, K. G. Lamb, and K. A. Scott, Asymmetries in gravity currents attributed to the nonlinear equation of state, J. Fluid Mech. **915**, A18 (2021).

[16] N. Castro-Folker, A. P. Grace, and M. Stastna, Three-dimensional structure of cold-water gravity currents, Phys. Rev. Fluids **8**, 113901 (2023).

[17] K. Bhavsar, M. Stastna, and N. Castro-Folker, Effects of weak buoyancy on shear instabilities in cold water, Phys. Rev. Fluids **11**, 023904 (2026).

[18] E. C. Carmack, C. B. Gray, C. H. Pharo, and R. J. Daley, Importance of lake-river interaction on seasonal patterns in the general circulation of Kamloops Lake, British Columbia, Limnol. Oceanogr. **24**, 634 (1979).

[19] K. B. Winters, P. N. Lombard, J. J. Riley, and E. A. D'Asaro, Available potential energy and mixing in density-stratified fluids, J. Fluid Mech. **289**, 115 (1995).

[20] C.-C. P. Caulfield and W. R. Peltier, The anatomy of the mixing transition in homogeneous and stratified free shear layers, J. Fluid Mech. **413**, 1 (2000).

[21] K. B. Winters, H. N. Ulloa, A. Wüest, and D. Bouffard, Energetics of radiatively heated ice-covered lakes, Geophys. Res. Lett. **46**, 8913 (2019).

[22] R. Tailleux, Negative available potential energy dissipation as the fundamental criterion for double diffusive instabilities, J. Fluid Mech. **994**, A5 (2024).

[23] R. Tailleux, On the energetics of stratified turbulent mixing, irreversible thermodynamics, Boussinesq models and the ocean heat engine controversy, J. Fluid Mech. **638**, 339 (2009).

[24] R. Tailleux, Local available energetics of multicomponent compressible stratified fluids, J. Fluid Mech. **842**, R1 (2018).

[25] J. Nycander, Energy conversion, mixing energy, and neutral surfaces with a nonlinear equation of state, J. Phys. Oceanogr. **41**, 28 (2011).

[26] C. J. Subich, K. G. Lamb, and M. Stastna, Simulation of the Navier-Stokes equations in three dimensions with a spectral collocation method, Int. J. Numer. Methods Fluids **73**, 103 (2013).

[27] A. P. Grace, M. Stastna, K. G. Lamb, and K. A. Scott, Gravity currents in the cabbeling regime, Phys. Rev. Fluids **8**, 014502 (2023).

[28] T. J. McDougall, D. R. Jackett, D. G. Wright, and R. Feistel, Accurate and computationally efficient algorithms for potential temperature and density of seawater, J. Atmos. Ocean. Technol. **20**, 730 (2003).

[29] A. P. Grace, A. Fogal, and M. Stastna, Restratification in late winter lakes induced by cabbeling, Geophys. Res. Lett. **50**, e2023GL103402 (2023).

[30] A. Cortés and S. MacIntyre, Mixing processes in small Arctic lakes during spring, Limnol. Oceanogr. **65**, 260 (2020).

[31] J. Olsthoorn, E. W. Tedford, and G. A. Lawrence, Salt-fingering in seasonally ice-covered lakes, Geophys. Res. Lett. **49**, e2022GL097935 (2022).

[32] T. Hanson, M. Stastna, and A. Coutino, Stratified shear instability in the cabbeling regime, Phys. Rev. Fluids **6**, 084802 (2021).

[33] J. Leyrer, H. Ulloa, J. Ortega, and J. Letelier, Onset of cabbeling instabilities in superconfined two-fluid systems, Phys. Fluids **36**, 126613 (2024).

[34] J. Letelier, H. Ulloa, J. Leyrer, and J. Ortega, Scaling CO_2-brine mixing in permeable media via analogue models, J. Fluid Mech. **962**, A8 (2023).

[35] E. Carmack and S. Vagle, Thermobaric processes both drive and constrain seasonal ventilation in deep Great Slave Lake, Canada, J. Geophys. Res.: Earth Surf. **126**, e2021JF006288 (2021).

[36] J. I. Bisits, J. D. Zika, and T. Sohail, Cabbeling as a catalyst and driver of turbulent mixing, J. Fluid Mech. **1011**, A17 (2025).

[37] D. J. Allum, A. P. Grace, and M. Stastna, Two-dimensional simulations of flow in ice-covered lakes with horizontal variations in surface albedo, Phys. Rev. Fluids **7**, 103501 (2022).